Overcomplete quantum tomography of a path-entangled two-photon state

L. De Santis,[1,*] G. Coppola,[1] C. Antón,[1] N. Somaschi,[1] C. Gómez,[1] A. Lemaître,[1] I. Sagnes,[1] L. Lanco,[1,2] J. C. Loredo,[1] O. Krebs,[1,†] and P. Senellart[1,‡]

[1]*Centre de Nanosciences et de Nanotechnologies, CNRS, Université Paris-Sud, Université Paris-Saclay, UMR 9001, 10 Boulevard Thomas Gobert, 91120 Palaiseau, France*

[2]*Université Paris Diderot 7, Physics Department, 75205 Paris Cedex 13, France*

(Received 24 July 2017; published 12 February 2019)

Path-entangled N-photon states are key resources for quantum enhanced metrology and quantum imaging, as well as quantum computation. However, the quantum tomography of path-entangled indistinguishable photons is still in its infancy. We propose and implement a quantum tomographical method to characterize path-entangled two-photon NOON states, which can be extended to arbitrary N. To access both the populations and the coherences of the path-encoded density matrix, a single ancilla spatial mode is introduced, and photon correlations are performed as a function of a single phase within an interferometer. We characterize a two-photon state generated through the Hong-Ou-Mandel interference of indistinguishable single photons emitted by a semiconductor quantum dot and show that an overcomplete data set reveals spatial coherences that could be otherwise hidden due to limited statistics. We finally extract the truly indistinguishable part of the density matrix and identify the main origin for the reduced degree of entanglement.

DOI: 10.1103/PhysRevA.99.022312

I. INTRODUCTION

Path entanglement is an important resource in the field of precision measurements, where the use of entangled particles provides accuracy beyond the standard quantum limit. A textbook example is the quantum enhanced optical phase measurement [1], which has already shown important applications in the field of microscopy [2–4], lithography [5,6], biological sensing [7,8], as well as gravitational-wave detection [9]. The quantum advantage arises from the use of path entanglement in interferometric protocols. For instance, a path-entangled N-photon state in the form of $|N0\rangle + e^{i\phi}|0N\rangle$, referred to as a NOON state, enables an N-fold enhancement in the phase resolution with a measurement sensitivity of $\Delta\phi = \frac{1}{N}$, beyond the standard quantum limit of $\Delta\phi = \frac{1}{\sqrt{N}}$ [10]. Path entanglement has also been proposed as a resource for quantum computing, both for intermediate, i.e., nonuniversal, tasks like Boson sampling [11], as well as for universal quantum computation using quantum walks of indistinguishable particles [12–14].

Various schemes are proposed to generate NOON states using beam splitters, ancillary photons, and postselection for path-entangled states [15,16], or through mixing quantum and classical light for polarization entangled states [17,18]. Today's state of the art consists of $N = 5$ photon NOON states [19] with most demonstrations using polarization encoding protocols [10,20]. Indeed, while path encoding offers great potential, it requires a phase control that is challenging to implement with bulk optics. Recent integrated photonics architectures have enabled the generation of on-chip path entanglement [21–24], thus benefiting from robust and precise phase control and reconfigurability [25]. However, the quantum tomography of multiphoton path-entangled states has been scarcely addressed so far. The tomography of a path-entangled single photon can be achieved using quantum homodyne tomography [26] and entanglement witnesses have been derived for two paths [27,28] and were recently extended to multiple paths [29]. Path entanglement of two photons has been demonstrated on chip, making use of a path-encoded controlled NOT (CNOT) gate [21] or the equally low probability of generating a photon pair in two nonlinear crystals [22]. In both cases the quantum tomography was achieved for *distinguishable* two-photon states and was mostly intended to quantify the chip performance rather than being an in-depth characterization of the produced state.

The most natural way of obtaining a two-photon path-entangled NOON state is to perform the Hong-Ou-Mandel (HOM) experiment [30] with perfectly indistinguishable single photons: by impinging on the two inputs of a balanced beam splitter, they interfere and leave the beam splitter in a maximally entangled state—a textbook experiment that has been realized with both heralded [10,31] and on-demand single-photon sources [32,33]. The creation of a two-photon NOON state has commonly been supported through the observation of the expected phase dependence for coincidences measured at the output of a Mach-Zehnder interferometer. Only recently, a full reconstruction of the two-photon NOON state has been achieved using homodyne tomography [34,35]; however, it was at the cost of using a local oscillator for each photon.

Here, we propose a method to obtain the density matrix of indistinguishable two-photon two-path states using coincidence detection on single-photon avalanche diodes. It

*Present address: Department of Electrical Engineering and Computer Science, Massachusetts Institute of Technology, Cambridge, Massachusetts 02139, USA

†olivier.krebs@c2n.upsaclay.fr

‡pascale.senellart-mardon@c2n.upsaclay.fr

relies on a single ancilla mode and the control of a single phase in a split Mach-Zehnder interferometer. We discuss the accuracy of standard tomography techniques and show how an overcomplete set of measurements enables one to confidently extract all coherences that could be otherwise hidden because of poor statistics. By exploiting the bosonic nature of photons as proposed by Adamson and co-workers [36], we extend our approach to assess the contribution of partially distinguishable photons to the density matrix, which brings insight into the cause for nonmaximal entanglement. Finally, we show how our method can be extended to arbitrary NOON states using the exact same scheme but photon-number-resolving detectors.

II. GENERATION OF THE TWO-PHOTON STATE

We use a recently developed semiconductor source of highly indistinguishable single photons [37] to generate a two-photon path-entangled state. The device consists of an electrically controlled single InGaAs quantum dot (QD) inserted in an optical cavity and placed in a cryostat at 8 K [see Fig. 1(a)]. The QD exciton transition is resonantly excited with 15-ps laser pulses at 82 MHz repetition rate. The transition is driven to its excited state using a π pulse controlled through the laser intensity. The resonant fluorescence photons are collected in a crossed polarization scheme so as to separate them from the excitation laser and are subsequently coupled to a single-mode optical fiber. Figure 1(d) shows the coincidence counts obtained when measuring the second-order autocorrelation function $g^{(2)}(t)$ with two single-photon detectors at the outputs of a fiber-based beam splitter. The very small area of the peak at zero delay gives $g^{(2)}(0) = 0.03 \pm 0.01$, evidencing the excellent single-photon purity of the source. Note that this residual signal arises mostly from scattered laser light since no spectral filtering was used in contrast to Ref. [37]. To create the two-photon path-entangled state in a HOM configuration, two photons successively generated 12.2 ns apart are first probabilistically routed on both outputs of a free-space polarizing beam splitter (PBS) [see Fig. 1(a)]. A 12.2-ns fiber-based delay line is added to one of the arms in order to temporally overlap both photons on the fiber-based HOM beam splitter (BS_{HOM}), which provides an excellent spatial-mode overlap of 0.997 and well-balanced reflection and transmission coefficients $R = 0.508$ and $T = 0.492$. For perfectly indistinguishable photons, the two photons should exit the beam splitter in the maximally entangled two-photon state $|\psi_{2002}\rangle = \frac{1}{\sqrt{2}}(|2,0\rangle - |0,2\rangle)$, where the first (second) number refers to the photon number in path 0 (path 1) [see Fig. 1(b)]. Directing the signal of the two output path modes 0 and 1 towards single-photon detectors leads to the standard experimental configuration used to measure the mean wave-packet overlap of the two photons. The corresponding coincidence histogram is shown in Fig. 1(e) from which a HOM visibility of 0.945 is deduced (for details on the procedure, see Ref. [38]), corresponding to a mean wave-packet overlap of 0.975 when correcting for the imperfect $g^{(2)}(0)$. The same device with a time delay between generated photons of 3 ns [38] and filtering the zero phonon line [39] delivers photons with indistinguishability beyond 0.98. We operate it here at longer delay and without spectral filtering in order to test the potential of the proposed tomography methods to measure deviations from the ideal NOON state.

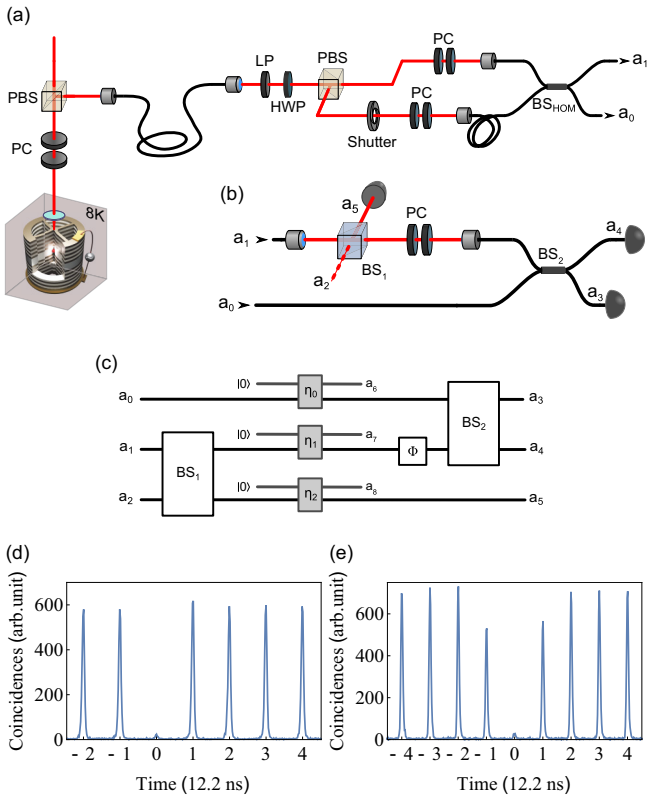

FIG. 1. (a) Schematic of the experimental setup used to generate the path-entangled two-photon state. LP stands for linear polarizer, HWP for half-wave plate, BS for beam splitter, PBS for polarizing beam splitter, and PC for polarization control, which is composed by a half-wave plate and a quarter-wave plate. The shutter on the lower line is used to measure the phase in the tomography setup every 10 s. (b) Schematic of the tomography setup. In our implementation BS_1 has a splitting ratio of 40:60 while that of BS_2 is 50:50. (c) Mode diagram corresponding to the setup in (b), where ϕ is the phase shift between the two arms of the interferometer and the additional beam splitters η_i describe the experimental losses. (d) Measurement of the second-order correlation function $g^{(2)}(t)$ of the single-photon source. (e) Measurement of the mean wave packet overlap of two photons from the source. This same histogram provides the correlation rate $R_{0,1}$ as defined in Sec. III.

III. TWO-PHOTON TWO-PATH QUANTUM STATE TOMOGRAPHY

To characterize the state of two photons distributed over two paths, the state tomography is performed in the two-photon subspace of the Hilbert space, tracing out the contributions of vacuum and single-photon state arising from probabilistic routing and losses [35]. Considering that the two photons cannot be distinguished in any degrees of freedom other than their spatial mode, it is described by a 3×3 density matrix ρ^{in} in the $|2,0\rangle$, $|1,1\rangle$, $|0,2\rangle$ basis [36]. Tomographical reconstruction of NOON states has been addressed for two orthogonal polarization modes of one spatial mode [40,41], where all coherences can be derived using N-fold

coincidences and SU(2) transformations via phase retarders and wave plates. Such a scheme can in principle be transposed to path encoding, yet at the cost of stabilizing two independent optical phases: one phase in one path, and the other in an additional Mach-Zehnder interferometer needed to mimic a tunable beam splitter. Here, we propose an alternative approach based on a single phase and an ancillary spatial mode.

Figure 1(b) presents the proposed experimental setup and Fig. 1(c) the corresponding mode diagram. Photons in paths 0 and 1, corresponding to the creation operators $\hat{a}_0^\dagger$ and $\hat{a}_1^\dagger$, are sent to a final fiber-based beam splitter labeled BS_2 in a Mach-Zehnder configuration. Path 0 is directly coupled to one of the inputs of BS_2. A free-space beam splitter BS_1 is inserted on the other arm of the Mach-Zehnder to entangle path 1 with the ancillary mode, the path labeled 2. The free-space part between BS_1 and BS_2 is not optically stabilized, generating a slowly varying optical phase ϕ which is periodically measured. As shown below, a set of nine photon correlation measurements, from a proper combination of paths i and j, and for two different phases, rendering the correlation rates $R_{i,j}(\phi)$ for $0 \leqslant i, j \leqslant 5$, allows one to perform the quantum state tomography in the spatial mode basis.

This design derives from an analogy to the tomography of a polarization-entangled two-photon state [42] for which a minimal set of measurements, i.e., enabling the linear reconstruction of the density matrix, includes photon correlations between nonorthogonal polarizations. Mapping paths 0 and 1 to the polarization modes H and V, the above experimental configuration essentially mimics such correlation measurements. Detection on the output paths 3 and 4 accounts for the projection onto the $(H \pm e^{i\phi}V)/\sqrt{2}$ polarizations. Correlations such as $R_{3,4}$—without the additional BS_1—evidence a $\cos 2\phi$ dependence, and have previously been used to confirm the nature of a two-photon NOON state [32]. Yet a complete polarization tomography must also include correlations such as $R_{i,5}$ with $i = 3, 4$, which in the polarization analogy correspond to correlation between linearly polarized photon V and diagonal or circular polarizations.

To derive the density matrix from a complete set of measurements, we first consider the case of a pure input state,

$$\begin{aligned} |\psi\rangle^{\text{in}} &= \alpha|2,0\rangle + \beta|1,1\rangle + \gamma|0,2\rangle \\ &= \left(\frac{\alpha}{\sqrt{2}}\hat{a}_0^\dagger\hat{a}_0^\dagger + \beta\hat{a}_0^\dagger\hat{a}_1^\dagger + \frac{\gamma}{\sqrt{2}}\hat{a}_1^\dagger\hat{a}_1^\dagger\right)|0_0,0_1\rangle, \end{aligned} \quad (1)$$

and the corresponding density matrix ρ^{in}. The diagonal terms corresponding to the populations can be obtained from the correlation rates $R_{0,1}$ for $|1,1\rangle$, $R_{0,0}$ for $|2,0\rangle$, and $R_{1,1}$ for $|0,2\rangle$, where $R_{i,j} = \langle\psi_{\text{in}}|\hat{a}_i^\dagger\hat{a}_j^\dagger\hat{a}_j\hat{a}_i|\psi_{\text{in}}\rangle$ refers to correlation counts obtained by coupling paths i and j to detectors. Without the use of photon-number-resolving detectors, the autocorrelation rate $R_{i,i}$ is obtained by coupling the path i to a beam splitter and performing a correlation measurement on the two outputs of this additional beam splitter. The population of the $|1,1\rangle$ state ranges from zero, in the case of perfectly indistinguishable photons, to 0.5, for fully distinguishable ones. We make use of the unitary transformation between modes 0, 1, and 2 and modes 3, 4, and 5, which is determined by the optical setup:

$$\begin{pmatrix}\hat{a}_3^\dagger\\ \hat{a}_4^\dagger\\ \hat{a}_5^\dagger\end{pmatrix} = U_{\text{setup}}\begin{pmatrix}\hat{a}_0^\dagger\\ \hat{a}_1^\dagger\\ \hat{a}_2^\dagger\end{pmatrix}. \quad (2)$$

This allows one to calculate the output state $|\psi_{\text{out}}\rangle$ and the corresponding correlation rates $R_{i,j} = \langle\psi_{\text{out}}|\hat{a}_i^\dagger\hat{a}_j^\dagger\hat{a}_j\hat{a}_i|\psi_{\text{out}}\rangle$ as a function of the density matrix elements $\rho_{k,l}^{\text{in}}$. By doing so, a minimal set of correlation measurements $R_{\text{comp.}}(\phi_1, \phi_2)$ is obtained when measuring the following rates for two distinct phases ϕ_1 and ϕ_2:

$$\begin{aligned} R_{\text{comp.}}(\phi_1,\phi_2) = (&R_{0,0}, R_{0,1}, R_{1,1}, \\ &\times R_{3,3}(\phi_1), R_{3,4}(\phi_1), R_{4,5}(\phi_1), \\ &\times R_{3,3}(\phi_2), R_{3,4}(\phi_2), R_{4,5}(\phi_2)) \end{aligned} \quad (3)$$

with $|\phi_1 - \phi_2| \neq 0, \frac{\pi}{2}, \pi$. The corresponding linear transformation matrix M relating $R_{\text{comp.}}$ to the vectorial form of ρ^{in} is invertible so that the density matrix of the analyzed state is deduced from correlation measurements through the linear equation

$$(\rho^{\text{in}}) = M^{-1}R_{\text{comp.}}(\phi_1,\phi_2). \quad (4)$$

The same relation holds for any mixed input state for which the density matrix is a linear superposition of pure-state density matrices weighted by the corresponding state probability.

In practice, some optical losses on the setup should be considered to correctly reproduce the measured correlations. These losses are modeled as additional beam splitters, labeled η_i for $i = 0, 1, 2$ as shown in Fig. 1(c), and respectively describe imperfect fiber-to-fiber coupling at one input of BS_2, insertion losses in free space to fiber coupling at the other input of BS_2, and losses on BS_1. For the analysis presented in the rest of this paper, we have extended the transformation of Eq. (2) to include the three additional optical modes required to account for the losses, in such a way that U_{setup} effectively reproduce the scheme of Fig. 1(c). Such an approach allows one to maintain a unitary description of the experiment and keep the same procedure as described above, at the cost of introducing more modes.

The calculated coincidence rates are shown in Fig. 2 for various input states in order to illustrate the sensitivity of the corresponding measurements. In the case of the ideal maximally entangled state $|\psi_{2002}\rangle$ (solid lines), both coincidence count rates $R_{3,4}$ and $R_{3,3}$ are expected to vary with 2ϕ, reflecting the enhanced phase resolution of the NOON state in the Mach-Zehnder interferometer. The maximum contrast and the horizontal shift of the interference pattern are determined by the amplitude and the phase of the coherence terms between $|0,2\rangle$ and $|2,0\rangle$. Note that, in our setup, the visibility of the interference for an ideal NOON state cannot reach a unit value due to the presence of the beam splitter BS_1 in one arm, as well as additional losses. For a fully mixed two-photon state (dotted lines), all coincidences show no dependence on ϕ (overlapping dotted red and blue lines for $R_{3,4}$ and $R_{3,3}$). The dashed line shows the calculated rates for the pure state $|\psi\rangle^{\text{in}} = \frac{\cos(\theta)}{\sqrt{2}}|2,0\rangle + \sin(\theta)e^{i\frac{\pi}{4}}|1,1\rangle - \frac{\cos(\theta)}{\sqrt{2}}|0,2\rangle$, with

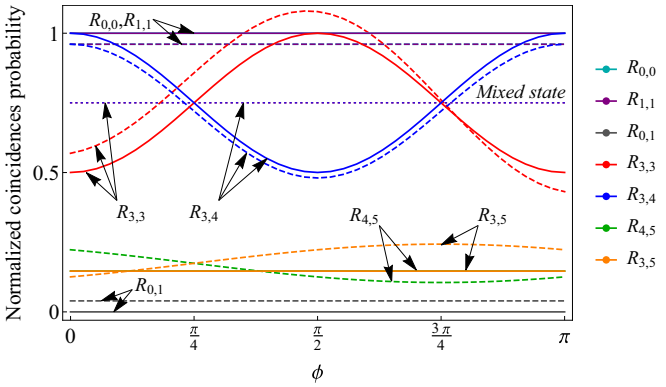

FIG. 2. Expected results from the measurements presented in the text for different input states. Solid lines denote calculated correlation rates for the ideal two-photon state $|\psi\rangle^{\text{in}} = \frac{1}{\sqrt{2}}(|2,0\rangle + |0,2\rangle)$. Dotted lines denote calculated correlation rates for the mixture $\rho^{\text{in}} = \frac{1}{2}|2,0\rangle\langle 2,0| + \frac{1}{2}|0,2\rangle\langle 0,2|$. In this case $R_{3,4} = R_{3,3}$ is independent on ϕ. Dashed lines denote calculated correlation rates corresponding to the state $|\psi\rangle^{\text{in}} = \frac{\cos(\theta)}{\sqrt{2}}|2,0\rangle + \sin(\theta)e^{i\frac{\pi}{4}}|1,1\rangle - \frac{\cos(\theta)}{\sqrt{2}}|0,2\rangle$, with $\theta = 0.2$.

$\theta = 0.2$. The presence of a $|1,1\rangle$ population results in a $\cos\phi$ dependence of $R_{3,5}$ and $R_{4,5}$ shifted by its initial phase—$\pi/4$ in the present example—which, as expected, does not shows an enhanced phase resolution. Analogously to $R_{3,4}$ and $R_{3,3}$, the interference pattern on the measurements of the type $R_{i,5}$ allows accessing the phase and amplitude of the coherence terms now relating $|1,1\rangle$ to the rest of the state. By combining all the measurements listed in Eq. (3) then, we are able to access all the elements of the density matrix of the analyzed state.

IV. OVERCOMPLETE SET OF MEASUREMENTS

To obtain the correlation rates $R_{3,4}$, $R_{3,5}$, and $R_{4,5}$, we use the experimental configuration sketched in Fig. 1(b). The phase ϕ in the interferometer arm freely evolves over time and correlation counts are continuously acquired. The phase is measured every 10 s by closing one input path of the HOM beam splitter BS_{HOM} using an electronically controlled shutter so that only one photon enters the analysis setup. The intensity signal recorded on path 3 or 4 is due to the single-photon interference and oscillates with ϕ, giving access to its time dependence. Figure 3(a) shows the time trace of the corresponding signal recorded over a 10-h period. It shows large fluctuations of $\cos(\phi)$ indicating that 2π variations of ϕ take place over a typical 10-min timescale. Figure 3(b) shows the corresponding histogram of total acquisition times distributed over 20 phase bins, showing a reasonably flat dependence with ϕ.

Three detectors are used on paths 3, 4, and 5 to record the three detection counts simultaneously. Time tagging of the events on the three detectors is recorded with respect to the laser trigger in order to reconstruct the correlation rates as a function of ϕ. To remove the errors due to fluctuations of the signal over time—arising from mechanical fluctuations in the relative laser spot-source overlap—the coincidence counts of each measurement are normalized. Normalization is achieved

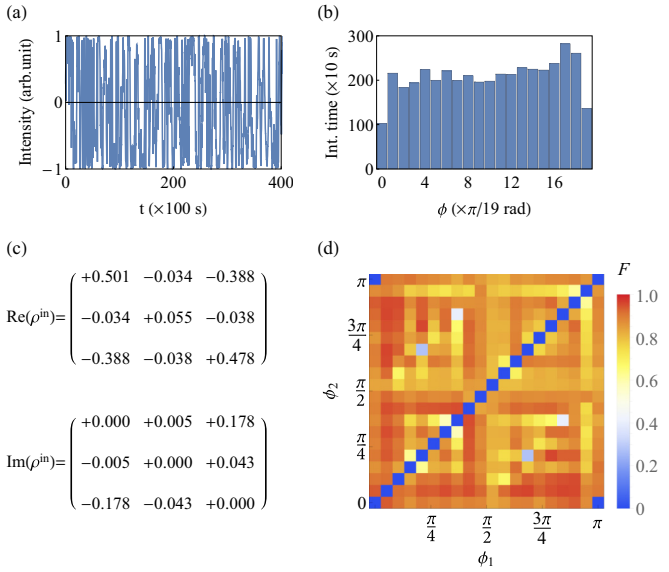

FIG. 3. (a) Single-photon rate giving access to the phase ϕ in the tomography setup, measured as a function of time on path 3 when blocking the lower path in Fig. 1(a). (b) Corresponding histogram of the acquisition time periods as a function of 20 phase bins. (c) Real and imaginary parts of the density matrix deduced from a set of nine measurements using the linear inversion tomography for $(\phi_1, \phi_2) = (0, \frac{5\pi}{19})$. (d) Fidelity to the maximally entangled NOON state deduced from the maximum-likelihood method with nine measurements as a function of (ϕ_1, ϕ_2).

with the correlation peaks recorded at time delays corresponding to multiples of the laser repetition period ($k \times 12$ ns) with $|k| \geqslant 2$. These peaks are due to single-photon events arising from different excitation pulses, and their magnitude can also be theoretically predicted from the product of single detection rates $R_j = \langle\psi_{\text{out}}|\hat{a}_j^\dagger \hat{a}_j|\psi_{\text{out}}\rangle$.

V. STANDARD QUANTUM TOMOGRAPHY

We first use the standard linear tomography approach, making use of Eq. (4). As discussed by Thew and coauthors, linear quantum tomography does not require that the projectors forming a complete set of measurements are orthogonal [43]. Mathematically, we find that for any couple of phases such that $|\phi_1 - \phi_2| \neq 0, \frac{\pi}{2}, \pi$, the measurement set $R_{\text{comp.}}(\phi_1, \phi_2)$ allows a reconstruction of the density matrix. Indeed, we note that for instance $(\phi_1, \phi_2) = (\frac{\pi}{4}, \frac{3\pi}{4})$ does not allow discriminating between the ideal NOON state from the totally mixed state (see solid and dotted lines in Fig. 2). In this case, R_{34} and R_{44} turn out to be only sensitive to the imaginary part of the coherence. In order to determine with the same precision the real and imaginary parts of all coherences, an optimal choice providing the lowest uncertainties in the state tomography is found for a couple of phases such that $|\phi_2 - \phi_1| \approx \frac{\pi}{4}$.

As an example, we derive the raw density matrix obtained for $(\phi_1, \phi_2) = (0, \frac{5\pi}{19})$ in Fig. 3(c). It exhibits small deviations from a physical density matrix with $\text{Tr}(\rho^{\text{in}}) = 1.034 > 1$. To determine a meaningful value of fidelity, we normalize the unphysical state by the trace and obtain a fidelity to the ideal

$|\psi_{2002}\rangle$ state of $F = 0.85$. To avoid the issue of nonphysical properties of the resulting matrix [42], we use the maximum-likelihood approach and numerically determine nine parameters t_ν defining the physical density matrix $\rho^{\text{in}}(t_1, \ldots, t_9)$, to maximize the likelihood function

$$P(t_1, \ldots, t_9) = \prod_{\nu=1}^{9} \exp - \frac{R_\nu(t_1, \ldots, t_9) - R_\nu}{\sigma_\nu^2}, \qquad (5)$$

where $R_\nu(t_1, \ldots, t_9)$ are the expected coincidence rates for the test input state $\rho^{\text{in}}(t_1, \ldots, t_9)$, R_ν are the measured ones, and σ_ν is the standard deviation of the νth coincidence.

Figure 3(d) shows the fidelity to ρ_{2002} deduced using the maximum-likelihood method as a function of (ϕ_1, ϕ_2). Fluctuations in the pattern of Fig. 3(d) result from experimental noise and/or insufficient statistics. The fidelity drops in the vicinity of $(\phi_1, \phi_2) = (\pi/4, 3\pi/4)$ as expected from the discussion above. We have calculated the average value of the deduced fidelity as well as its standard deviation as a function of $|\phi_2 - \phi_1|$: no dependence is observed for the present set of measurements as long as $|\phi_2 - \phi_1| \neq 0$ and $|\phi_2 - \phi_1| \neq \frac{\pi}{2}$, where noise gives a strong threefold increase of the standard deviation. Away from these two singular points, the average fidelity is 0.87 with a standard deviation of 0.06.

VI. OVERCOMPLETE QUANTUM TOMOGRAPHY

The measured normalized coincidence count rates $R_{3,4}$, $R_{3,3}$, $R_{3,5}$, and $R_{4,5}$ are plotted in Fig. 4(a) as a function of ϕ, together with the phase-independent count rates $R_{0,0}$, $R_{0,1}$ and $R_{1,1}$. Experimental error bars are derived taking into account the Poissonian noise on the coincidences as well as on the normalization count rates. $R_{3,3}$ shows stronger noise due to the lower statistics available for the measurement.

The dashed lines in Fig. 4(a) show the correlation rates calculated for the state deduced from linear tomography presented in Fig. 3(c), evidencing the limited accuracy of the standard tomography. Indeed, the corresponding correlations fail to reproduce the experimental ones on the full ϕ scale, particularly in the $[\frac{\pi}{2}, \pi]$ range, which is somehow expected since both ϕ_1 and ϕ_2 were chosen in the $[0, \frac{\pi}{2}]$ range.

To obtain a better insight into the two-photon state, the likelihood function is now maximized for the whole set of 79 phase-dependent measurements. The density matrix of the corresponding input state ρ_{over} is shown in Figs. 4(b) and 4(c). It presents a fidelity to the NOON state of 0.91 ± 0.02, in the range of the average fidelity obtained through nine measurements within the standard deviation. The coincidence rates corresponding to this reconstructed state are superimposed on the measurements in Fig. 4(a) (solid lines), showing a very good agreement with the experimental observations. The observed small phase dependence of $R_{4,5}$ and $R_{3,5}$ is well accounted for, evidencing coherence between the $|1, 1\rangle$ and the $|0, 2\rangle$ and $|2, 0\rangle$ terms.

This analysis shows that the use of an overcomplete tomography allows for any state reconstruction without prior assumption about the state. Indeed, as shown in Fig. 2, the coherences between the $|0, 2\rangle$ and $|2, 0\rangle$ as well as the coherence between the $|1, 1\rangle$ and the $|2, 0\rangle$ or $|0, 2\rangle$ components lead to a horizontal shift in the phase-dependent correlation

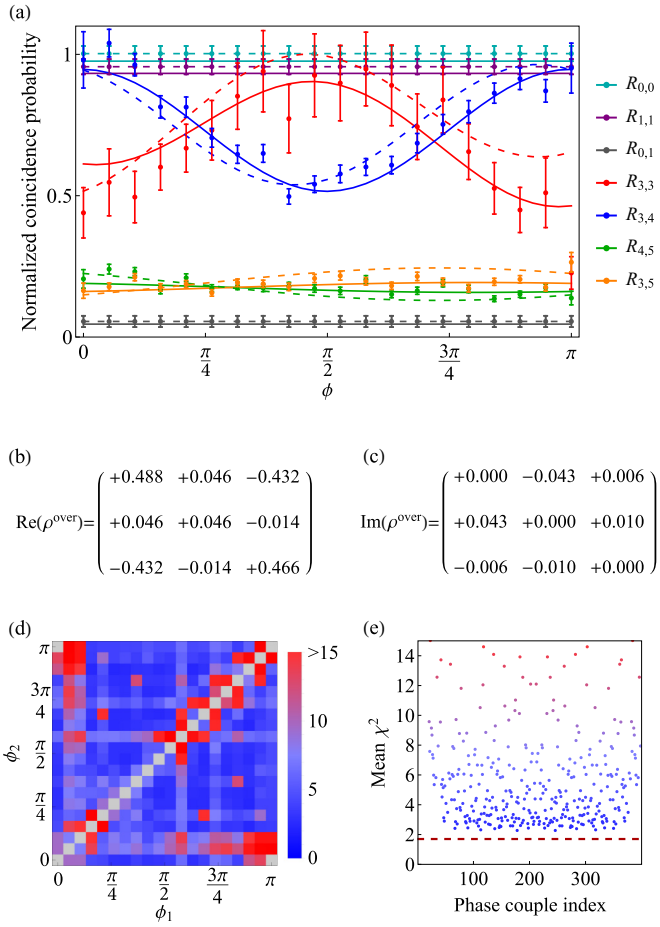

FIG. 4. (a) Normalized coincidence rates as a function of ϕ. Symbols denote measurements. Dotted lines denote calculated coincidence rates for the state deduced from linear tomography for $(\phi_1, \phi_2) = (0, \frac{\pi}{4})$ [see Fig. 3(d)]. Solid lines denote coincidence rates calculated for the state deduced from the overcomplete set of 79 measurements. (b) Real and (c) imaginary part of the density matrix deduced from an overcomplete set of 79 measurements. (d) Mean χ^2 between the measured correlation rates over the full ϕ range and the expected ones for the state deduced for each phase couple (ϕ_1, ϕ_2) using the maximum-likelihood method. (e) Mean χ^2 as a function of an index representing the 200 phase couples (ϕ_1, ϕ_2). The horizontal dashed line shows the mean χ^2 value of 1.7 obtained for the state reconstructed with the overcomplete data set.

rates. As a result, without prior hypothesis or knowledge on the state, one cannot *a priori* identify a phase couple (ϕ_1, ϕ_2) that would allow for a reliable state reconstruction using the single set of nine measurements. To illustrate this quantitatively, Fig. 4(d) shows the mean χ^2 between the measured correlation rates over the full ϕ range and the expected ones for the state deduced for all phase couples (ϕ_1, ϕ_2) using the maximum-likelihood method. Figure 4(e) shows the same mean χ^2 as a function of an index representing the 200 phase couples (ϕ_1, ϕ_2) evidencing a mean χ^2 larger for any couple of phase (ϕ_1, ϕ_2) than the value of 1.7 obtained for the state reconstructed with the overcomplete data set, shown by the horizontal line. The use of an overcomplete data set, monitoring the whole phase dependence, allows for reliable

reconstruction of any arbitrary state. In the next section, we extend our analysis a step further to obtain a diagnosis for the deviation of the produced state from the ideal NOON state.

VII. EXTRACTING THE TRUE PHOTON INDISTINGUISHABILITY

The creation of a maximally entangled two-photon NOON state depends on various parameters: the indistinguishability of the photons impinging on the HOM beam splitter, the balance of the reflection and transmission coefficients, as well as any undesired source of background light. On the one hand, the interference of two perfectly indistinguishable photons on an unbalanced beam splitter, with $|R| \neq |T|$, results in a $|1,1\rangle$ population. On the other hand, two distinguishable photons create a $|1,1\rangle$ population with a perfectly balanced beam splitter. In any case, the distinguishability of the photons affects coherences between $|2,0\rangle$ and $|0,2\rangle$ only via the reduction of their populations. In the present experiment—using a semiconductor quantum dot operated without any spectral filtering of the zero-phonon line—two origins for the photon distinguishability can be expected. First, a residual phonon sideband emission certainly takes place and slightly reduces the photon indistinguishability, as recently shown [39]. Additionally, the resonant excitation scheme leads to a small fraction of residual laser light not completely suppressed in the crossed polarized collection. This residual light is also distinguishable from the single photons emitted by the quantum dot and is also responsible for the measured nonzero $g^{(2)}(0)$ shown in Fig. 1(d).

Even though the physical origin of each detected photon cannot be determined by our apparatus used for tomography, Adamson and co-workers have demonstrated that in such a situation it is still possible to extract more information on the two-photon state [36]. The contribution of the truly distinguishable photons to the $|1,1\rangle$ population can be separated from that due to an imperfect setup via a more refined analysis of the visible and hidden degrees of freedom of the state. In practice, one introduces the four-state basis $|2,0\rangle$, $|0,2\rangle$, ψ^+, ψ^-, corresponding to the visible degree of freedom, where the $\psi^\pm$ are now the symmetric and antisymmetric states of two possibly distinguishable photons "a" and "b" on each path: $\psi^\pm = \frac{|1_a,1_b\rangle \pm |1_b,1_a\rangle}{\sqrt{2}}$. Truly indistinguishable photons can only occupy the symmetric state ψ^+; thus any population in the antisymmetric state ψ^- reveals the presence of distinguishing information. The 4×4 density matrix ρ^{vis} reads in this basis [31,36]

$$\rho^{\mathrm{vis}} = \begin{pmatrix} \rho_{20,20} & \rho_{20,\psi^+} & \rho_{20,02} & 0 \\ \rho_{\psi^+,02} & \rho_{\psi^+,\psi^+} & \rho_{02,\psi^+} & 0 \\ \rho_{02,20} & \rho_{\psi^+,02} & \rho_{02,02} & 0 \\ 0 & 0 & 0 & \rho_{\psi^-,\psi^-} \end{pmatrix} = \begin{pmatrix} (\rho^+_{k,l}) & 0 \\ 0 & \rho^- \end{pmatrix}, \tag{6}$$

where the coherences between the 3×3 symmetric ρ^+ and 1×1 antisymmetric ρ^- subspaces are zero. By considering a pure input state in the form

$$|\psi\rangle^{\mathrm{in}} = (\alpha \hat{a}^\dagger_{0,a}\hat{a}^\dagger_{0,b} + \beta \hat{a}^\dagger_{0,a}\hat{a}^\dagger_{1,b} + \gamma \hat{a}^\dagger_{0,b}\hat{a}^\dagger_{1,a} + \delta \hat{a}^\dagger_{1,a}\hat{a}^\dagger_{1,b})|0\rangle$$

$$\rho^{\mathrm{vis}} = \begin{pmatrix} 0.486+0.000\,i & 0.032-0.007\,i & -0.434+0.011\,i & 0.000 \\ 0.032+0.007\,i & 0.007+0.000\,i & -0.015+0.010\,i & 0.000 \\ -0.434-0.011\,i & -0.015-0.010\,i & 0.467+0.000\,i & 0.000 \\ 0.000 & 0.000 & 0.000 & 0.040+0.000\,i \end{pmatrix}$$

FIG. 5. The 4×4 density matrix with the distinguishable and indistinguishable parts of the two-photon state.

and calculating the corresponding coincidences

$$R_{i,j} = \langle \psi_{\mathrm{out}}|\hat{a}^\dagger_{i,a}\hat{a}^\dagger_{j,b}\hat{a}_{j,b}\hat{a}_{i,a} + \hat{a}^\dagger_{i,b}\hat{a}^\dagger_{j,a}\hat{a}_{j,a}\hat{a}_{i,b}|\psi_{\mathrm{out}}\rangle,$$

we can determine new relations between $(\rho^+_{k,l}, \rho^-)$ and the $R_{i,j}$ terms. We observed that, as expected, the calculated $R_{i,j}$ do not formally depend on the coherence terms between the symmetric and antisymmetric part of the density matrix, even if they are considered as nonzero. We then carry out the maximum-likelihood method using the overcomplete set of measurements to obtain the ten parameters defining the physical density matrix in the form of ρ^{vis} (see Fig. 5). Notably, most of the $|1,1\rangle$ population now appears on the antisymmetric part ρ_{ψ^-,ψ^-} of the density matrix, with a negligible population on the symmetric ρ_{ψ^+,ψ^+} population. This approach allows us to ascribe most of the NOON state imperfection to a partial distinguishability of the photons and not to imperfections in the HOM beam splitter. Furthermore, knowing that the lower bound of $\rho_{\psi^+,\psi^+} + \rho_{\psi^-,\psi^-}$ is given by $g^{(2)}(0) = 0.03$, we ascribe most of the extracted distinguishability to the residual laser.

VIII. EXTENSION TO HIGH PHOTON NUMBERS

The present scheme can be extended to perform the tomography of high-photon-number NOON states by making use of photon-number-resolving (PNR) detectors. Such an approach allows one to access all the necessary Nth-order photon correlations as previously demonstrated for polarization-encoded NOON states [40,41].

Indeed, the possible distributions of N indistinguishable photons over two modes leads to a density matrix with $(N+1)^2$ elements for a NOON state. Introducing an ancillary mode, we obtain three accessible output modes over which the photons can be distributed, giving rise to $(N+2)(N+1)/2$ possible configurations for the photon-number distribution. Detecting each of these possible photon distributions for two different values of the interferometer phase gives a number of measurements exceeding the number of elements in the density matrix. The tomography problem is then reduced to the identification of two possible values of phases giving a complete set of measurements.

As an example, we consider explicitly here the case of $N=3$. The density matrix $\hat{\rho}_{3003}$ of the three indistinguishable photons distributed over the two modes $\hat{a}_0$ and $\hat{a}_1$ of the interferometer has 16 elements to be accessed in a basis consisting of $\{|3,0\rangle,\ |2,1\rangle,\ |1,2\rangle,\ |0,3\rangle\}$. We can define an ideal correlation measurement between n photons on the mode i and m photons on the mode j as $\hat{R}^{n,m}_{i,j} = |n\rangle\langle n| \otimes |m\rangle\langle m|$. The four populations can be measured using PNR detectors from

the correlations

$$\hat{R}^{3,0}_{0,1},\ \hat{R}^{2,1}_{0,1},\ \hat{R}^{1,2}_{0,1},\ \hat{R}^{0,3}_{0,1}.$$

Following the same procedure as before, by placing PNR detectors at the three outputs of the split Mach-Zehnder setup, six additional measurements can be performed, each for two different values (ϕ_1 and ϕ_2) of the interferometer phase ϕ. In this case, it can be shown that

$$\hat{R}^{3,0}_{3,4}(\phi),\ \hat{R}^{0,3}_{3,4}(\phi),\ \hat{R}^{2,1}_{3,4}(\phi),\ \hat{R}^{2,1}_{3,5}(\phi),\ \hat{R}^{1,2}_{4,5}(\phi),\ \hat{R}^{2,1}_{4,5}(\phi)$$

for $|\phi_1 - \phi_2| \neq k\frac{\pi}{2}, k\frac{\pi}{3}$, along with the four population measurements listed above, constitute a complete set of measurements for the linear reconstruction of the density matrix.

IX. CONCLUSIONS

In the present work, we have proposed a simple experimental method to perform quantum state tomography of a two-photon path-entangled state. Although unavoidable experimental noise led to uncertainties in a standard quantum tomography approach, we have shown that an overcomplete data set allows one to extract highly reliable information. Moreover, by accessing the indistinguishable and distinguishable parts of the density matrix, we provide a precise diagnosis for the deviation from an ideal state, separating limitations arising either from the photon source or from imperfections of the optical network.

High-photon-number path-entangled NOON states are foreseen as important resources for many applications, including quantum enhanced imaging, sensing, and lithography. A quantitative estimation of the degree of entanglement is thus a key resource, and while approaches are explored to detect entanglement at the lowest cost, full tomography may very well be the only reliable solution [44]. Here, we have proposed an approach that allows for the quantum tomography of path-encoded NOON states for any N by using a single and simple experimental setup.

ACKNOWLEDGMENTS

The authors are thankful to Professor Andrew G. White for stimulating discussions. This work was partially supported by the ERC Starting Grant No. 277885 QD-CQED, the French Agence Nationale pour la Recherche grant USSEPP, the French RENATECH network, the Marie Curie individual fellowships SQUAPH and SMUPHOS, a public grant overseen by the French National Research Agency (ANR) as part of the "Investissements d'Avenir" program (Labex NanoSaclay, reference ANR-10-LABX-0035), and the iXcore foundation.

[1] T. Nagata, R. Okamoto, J. L. O'Brien, K. Sasaki, and S. Takeuchi, Science **316**, 726 (2007).
[2] E. J. S. Fonseca, C. H. Monken, and S. Pádua, Phys. Rev. Lett. **82**, 2868 (1999).
[3] Y. Israel, S. Rosen, and Y. Silberberg, Phys. Rev. Lett. **112**, 103604 (2014).
[4] P. A. Morris, R. S. Aspden, J. E. C. Bell, R. W. Boyd, and M. J. Padgett, Nat. Commun. **6**, 5913 (2015).
[5] A. N. Boto, P. Kok, D. S. Abrams, S. L. Braunstein, C. P. Williams, and J. P. Dowling, Phys. Rev. Lett. **85**, 2733 (2000).
[6] M. D'Angelo, M. V. Chekhova, and Y. Shih, Phys. Rev. Lett. **87**, 013602 (2001).
[7] M. A. Taylor, J. Janousek, V. Daria, J. Knittel, B. Hage, H.-A. Bachor, and W. P. Bowen, Nat. Photon. **7**, 229 (2013).
[8] F. Wolfgramm, C. Vitelli, F. A. Beduini, N. Godbout, and M. W. Mitchell, Nat. Photon. **7**, 28 (2013).
[9] J. P. Dowling, Contemp. Phys. **49**, 125 (2008).
[10] M. W. Mitchell, J. S. Lundeen, and A. M. Steinberg, Nature (London) **429**, 161 (2004).
[11] S. Aaronson and A. Arkhipov, in *Proceedings of the 43rd Annual ACM Symposium on Theory of Computing—STOC '11* (ACM Press, New York, 2011), p. 333.
[12] A. M. Childs, D. Gosset, and Z. Webb, Science **339**, 791 (2013).
[13] J. K. Gamble, M. Friesen, D. Zhou, R. Joynt, and S. N. Coppersmith, Phys. Rev. A **81**, 052313 (2010).
[14] X. Qiang, T. Loke, A. Montanaro, K. Aungskunsiri, X. Zhou, J. L. O'Brien, J. B. Wang, and J. C. F. Matthews, Nat. Commun. **7**, 11511 (2016).
[15] G. J. Pryde and A. G. White, Phys. Rev. A **68**, 052315 (2003).
[16] H. Cable and J. P. Dowling, Phys. Rev. Lett. **99**, 163604 (2007).
[17] H. F. Hofmann and T. Ono, Phys. Rev. A **76**, 031806(R) (2007).
[18] L. Pezzé and A. Smerzi, Phys. Rev. Lett. **100**, 073601 (2008).
[19] I. Afek, O. Ambar, and Y. Silberberg, Science **328**, 879 (2010).
[20] A. G. White, D. F. V. James, P. H. Eberhard, and P. G. Kwiat, Phys. Rev. Lett. **83**, 3103 (1999).
[21] P. J. Shadbolt, M. R. Verde, A. Peruzzo, A. Politi, A. Laing, M. Lobino, J. C. F. Matthews, M. G. Thompson, and J. L. O'Brien, Nat. Photon. **6**, 45 (2011).
[22] J. W. Silverstone, R. Santagati, D. Bonneau, M. J. Strain, M. Sorel, J. L. O'Brien, and M. G. Thompson, Nat. Commun. **6**, 7948 (2015).
[23] M. Tillmann, S.-H. Tan, S. E. Stoeckl, B. C. Sanders, H. De Guise, R. Heilmann, S. Nolte, A. Szameit, and P. Walther, Phys. Rev. X **5**, 041015 (2015).
[24] N. Spagnolo, C. Vitelli, L. Aparo, P. Mataloni, F. Sciarrino, A. Crespi, R. Ramponi, and R. Osellame, Nat. Commun. **4**, 1606 (2013).
[25] A. Crespi, R. Osellame, R. Ramponi, D. J. Brod, E. F. Galvão, N. Spagnolo, C. Vitelli, E. Maiorino, P. Mataloni, and F. Sciarrino, Nat. Photon. **7**, 545 (2013).
[26] S. A. Babichev, J. Appel, and A. I. Lvovsky, Phys. Rev. Lett. **92**, 193601 (2004).
[27] O. Morin, J.-D. Bancal, M. Ho, P. Sekatski, V. D'Auria, N. Gisin, J. Laurat, and N. Sangouard, Phys. Rev. Lett. **110**, 130401 (2013).
[28] M. Ho, O. Morin, J.-D. Bancal, N. Gisin, N. Sangouard, and J. Laurat, New J. Phys. **16**, 055011 (2014).
[29] F. Monteiro, V. C. Vivoli, T. Guerreiro, A. Martin, J.-D. Bancal, H. Zbinden, R. T. Thew, and N. Sangouard, Phys. Rev. Lett. **114**, 170504 (2015).
[30] C. K. Hong, Z. Y. Ou, and L. Mandel, Phys. Rev. Lett. **59**, 2044 (1987).
[31] F. Wolfgramm, A. Cerè, and M. W. Mitchell, J. Opt. Soc. Am. B **27**, A25 (2010).

[32] A. J. Bennett, J. P. Lee, D. J. P. Ellis, T. Meany, E. Murray, F. F. Floether, J. P. Griffths, I. Farrer, D. A. Ritchie, and A. J. Shields, Sci. Adv. **2**, e1501256 (2016).
[33] M. Müller, H. Vural, C. Schneider, A. Rastelli, O. G. Schmidt, S. Höfling, and P. Michler, Phys. Rev. Lett. **118**, 257402 (2017).
[34] A. E. Ulanov, I. A. Fedorov, D. Sychev, P. Grangier, and A. I. Lvovsky, Nat. Commun. **7**, 11925 (2016).
[35] J.-I. Yoshikawa, M. Bergmann, P. van Loock, M. Fuwa, M. Okada, K. Takase, T. Toyama, K. Makino, S. Takeda, and A. Furusawa, Phys. Rev. A **97**, 053814 (2018).
[36] R. B. A. Adamson, L. K. Shalm, M. W. Mitchell, and A. M. Steinberg, Phys. Rev. Lett. **98**, 043601 (2007).
[37] N. Somaschi, V. Giesz, L. De Santis, J. C. Loredo, M. P. Almeida, G. Hornecker, S. L. Portalupi, T. Grange, C. Antón, J. Demory, C. Gómez, I. Sagnes, N. D. Lanzillotti-Kimura, A. Lemaítre, A. Auffeves, A. G. White, L. Lanco, and P. Senellart, Nat. Photon. **10**, 340 (2016).
[38] J. C. Loredo, N. A. Zakaria, N. Somaschi, C. Anton, L. de Santis, V. Giesz, T. Grange, M. A. Broome, O. Gazzano, G. Coppola, I. Sagnes, A. Lemaitre, A. Auffeves, P. Senellart, M. P. Almeida, and A. G. White, Optica **3**, 433 (2016).
[39] T. Grange, N. Somaschi, C. Antón, L. De Santis, G. Coppola, V. Giesz, A. Lemaître, I. Sagnes, A. Auffèves, and P. Senellart, Phys. Rev. Lett. **118**, 253602 (2017).
[40] U. Schilling, J. Von Zanthier, and G. S. Agarwal, Phys. Rev. A **81**, 013826 (2001).
[41] Y. Israel, I. Afek, S. Rosen, O. Ambar, and Y. Silberberg, Phys. Rev. A **85**, 022115 (2012).
[42] D. F. V. James, P. G. Kwiat, W. J. Munro, and A. G. White, Phys. Rev. A **64**, 052312 (2001).
[43] R. T. Thew, K. Nemoto, A. G. White, and W. J. Munro, Phys. Rev. A **66**, 012303 (2002).
[44] C. Carmeli, T. Heinosaari, A. Karlsson, J. Schultz, and A. Toigo, Phys. Rev. Lett. **116**, 230403 (2016).